Inorganic Chemistry
Article

Inorg. Chem. **2010**, *49*, 4611–4619 **4611**
DOI: 10.1021/ic100186v

Two-Electron Redox Energetics in Ligand-Bridged Dinuclear Molybdenum and Tungsten Complexes

Richard L. Lord,[†] Franklin A. Schultz,*[,†,‡] and Mu-Hyun Baik*[,†]

[†]*Department of Chemistry, Indiana University, 800 East Kirkwood Avenue, Bloomington, Indiana 47405, and* [‡]*Department of Chemistry and Chemical Biology, Indiana University−Purdue University Indianapolis, 402 North Blackford Street, Indianapolis, Indiana 46202*

Received January 29, 2010

Electron-transfer energetics of bridged dinuclear compounds of the form $[(CO)_4M(\mu\text{-}L)]_2^{0/1-/2-}$ (M = Mo, W; L = PPh_2^-, SPh^-) were explored using density functional theory coupled to a continuum solvation model. The experimentally observed redox potential inversion, a situation where the second of two electron transfers is more thermodynamically favorable than the first, was reproduced within this model. This nonclassical energy ordering is a prerequisite for the apparent transfer of two electrons at one potential, as observed in many biologically and technologically important systems. We pinpoint the origin of this phenomenon to be an unusually unfavorable electrostatic repulsion for the first electron transfer due to the redox noninnocent behavior of the bridging ligands. The extent of redox noninnocence is explained in terms of an orbital energy resonance between the metal−carbonyl and bridging ligand fragments, leading to a general mechanism by which potential inversion could be controlled in diamond-core dinuclear systems.

Introduction

Multiple-electron-transfer reactions are often critically important to chemical and biological processes including hydrogen production,[1−3] oxygen evolution,[4,5] and nitrogen fixation.[6,7] By transferring two redox equivalents in a concerted manner, bonds may be formed or cleaved while avoiding potentially damaging radical intermediates. In cyclic voltammetry, such a process is observed as a single voltammetric signal with a current response corresponding to two electrons. The prerequisite for this situation is that there must be a potential at which both the fully oxidized (eq 1) and intermediate species (eq 2) are reduced ($E^{\circ\prime}_{ii} > E^{\circ\prime}_{i}$), a situation commonly referred to as redox potential inversion. It is generally accepted that the simultaneous transfer of two electrons is infeasible, but details of the sequence by which the two-electron response arises depend on the amount of potential inversion.[8,9] When the magnitude of potential inversion is large, the second current equivalent can arise from rapid reduction of A^- before it can escape the region near the electrode surface by diffusion. When the magnitude of inversion is small, however, this species has time to diffuse away from the surface and undergo disproportionation (eq 3), affording a second equivalent of A, which is reduced at the given potential. Regardless of the details of the reaction sequence, apparent two-electron transfer poses a fundamental paradox.

$$A + e^- \leftrightarrows A^- \quad E^{\circ\prime}_{i}, k_{sh,i} \tag{1}$$

$$A^- + e^- \leftrightarrows A^{2-} \quad E^{\circ\prime}_{ii}, k_{sh,ii} \tag{2}$$

$$2A^- \leftrightarrows A + A^{2-} \quad \Delta G^{\circ}_{disp}, K_{disp} \tag{3}$$

Potential inversion implies that the second reduction, $A^- + e^- \rightarrow A^{2-}$, releases more energy than the first, $A + e^- \rightarrow A^-$, i.e., that the second reduction is easier than the first. Electrostatic arguments demand that adding the electron to an anion should intrinsically be more difficult than adding an electron to its neutral analogue, in accordance with the convexity principle (Figure 1, red line).[10,11] For systems with properly bound electrons, the stabilization energy upon addition of electrons should become smaller in magnitude with an increase in the number of electrons, a principle that is

*To whom correspondence should be addressed. E-mail: fschultz@iupui.edu (F.A.S.), mbaik@indiana.edu (M.-H.B.).

(1) Adams, M. W. W.; Stiefel, E. I. *Science* **1998**, *282*, 1842–1843.
(2) Evans, D. J.; Pickett, C. J. *Chem. Soc. Rev.* **2003**, *32*, 268–275.
(3) Vincent, K. A.; Parkin, A.; Armstrong, F. A. *Chem. Rev.* **2007**, *107*, 4366–4413.
(4) Yachandra, V. K.; Sauer, K.; Klein, M. P. *Chem. Rev.* **1996**, *96*, 2927–2950.
(5) Eisenberg, R.; Gray, H. B. *Inorg. Chem.* **2008**, *47*, 1697–1699.
(6) Howard, J. B.; Rees, D. C. *Chem. Rev.* **1996**, *96*, 2965–2982.
(7) Burgess, B. K.; Lowe, D. J. *Chem. Rev.* **1996**, *96*, 2983–3012.
(8) Evans, D. H. *Acta Chem. Scand.* **1998**, *52*, 194–197.
(9) Gileadi, E. *J. Electroanal. Chem.* **2002**, *532*, 181–189.
(10) Frost, A. A. *J. Am. Chem. Soc.* **1951**, *73*, 2680–2682.
(11) Parr, R. G.; Yang, W. *Density Functional Theory of Atoms and Molecules*; Oxford University Press: New York, 1989.

© 2010 American Chemical Society
Published on Web 04/20/2010

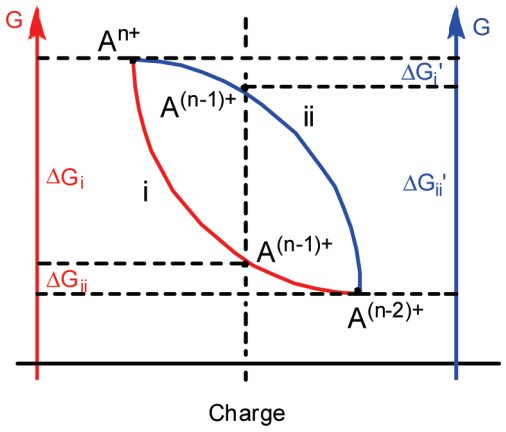

Figure 1. Energy diagram displaying normal ordering ($\Delta G_i < \Delta G_{ii}$), giving a convex curve (red), and abnormal ordering ($\Delta G_i' > \Delta G_{ii}'$), giving a concave curve (blue).

strictly adhered to by atoms in gas phase. Molecular systems in solution phase may violate the convexity principle by utilizing a number of chemical effects including a change of the structure or composition, ligation, protonation, or ion-pair formation to afford this nonclassical behavior.[12−15] Thus, the concept of how two-electron redox systems may be engineered is generically understood. The overall energy released upon acceptance of two electrons must be apportioned asymmetrically in favor of the second step to distort the relative energies, as shown in blue in Figure 1.

Despite this fairly clear conceptual picture, a detailed understanding of multielectron redox systems remains challenging. For example, the ligand-bridged molybdenum- and tungsten-based dinuclear systems illustrated in Scheme 1 exhibit a single two-electron transfer accompanied by cleavage of a metal−metal σ bond,[16−19] initiated by electron transfer into the metal−metal σ^* lowest unoccupied molecular orbital (LUMO), which is thought to provide the driving force for the single two-electron chemistry. Analogous behavior has been observed for related ligand-bridged

Scheme 1

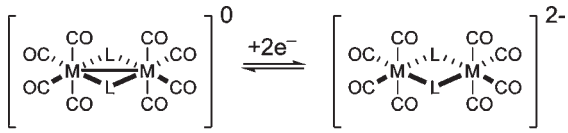

1: M = Mo, L = Ph_2P^- **3:** M = Mo, L = PhS^-
2: M = W, L = Ph_2P^- **4:** M = W, L = PhS^-

dinuclear compounds.[15,19−43] It is unclear, however, as to why and how the electrochemical cleavage of the metal−metal σ bond can give rise to the asymmetric energy distortion required for potential inversion. A number of counter-examples exist wherein stepwise one-electron transfer is observed in related systems. For example, two one-electron transfers separated by ca. 350 mV are observed for $[Fe_2(\mu\text{-}PPh_2)_2(C_5H_5)_2(CO)_2]^{2+/+/0}$,[44] although reduction of the metal−metal singly bonded dication populates the Fe−Fe σ^* antibonding orbital and lengthens the Fe−Fe distance by ∼0.7 Å.

$$[M^{I}{}_2(\mu\text{-}L)_2(CO)_8]^0 + 2e^- \leftrightharpoons [M^{0}{}_2(\mu\text{-}L)_2(CO)_8]^{2-} \quad E^{o\prime}{}_{obs} \tag{4}$$

$$(M = Mo, W; L^- = R_2P^-, RS^-)$$

Previously, we presented computational studies of multi-electron redox systems[42,43,45] based on density functional theory (DFT),[11,46] demonstrating that the solution phase free energy of disproportionation (eq 3) can be computed to a sufficient accuracy to provide a detailed explanation for two-electron redox chemistry. Once properly benchmarked

(12) Evans, D. H. *Chem. Rev.* **2008**, *108*, 2113–2144.
(13) Macias-Ruvalcaba, N. A.; Evans, D. H. *Chem.—Eur. J.* **2007**, *13*, 4386–4395.
(14) Evans, D. H.; Lehmann, M. W. *Acta Chem. Scand.* **1999**, *53*, 765–774.
(15) Schultz, F. A.; Lord, R. L.; Yang, X.; Baik, M.-H. In *ACS Symposium Series*; Long, E. C., Baldwin, M. J., Eds.; American Chemical Society: Washington, DC, 2009; Vol. 1012, pp 151−166.
(16) Smith, D. A.; Zhuang, B.; Newton, W. E.; McDonald, J. W.; Schultz, F. A. *Inorg. Chem.* **1987**, *26*, 2524–2531.
(17) Fernandes, J. B.; Zhang, L. Q.; Schultz, F. A. *J. Electroanal. Chem.* **1991**, *297*, 145–161.
(18) Hill, M. G.; Rosenhein, L. D.; Mann, K. R.; Mu, X. H.; Schultz, F. A. *Inorg. Chem.* **1992**, *31*, 4108–4111.
(19) Uhrhammer, D.; Schultz, F. A. *J. Phys. Chem. A* **2002**, *106*, 11630–11636.
(20) Dessy, R. E.; Weissman, P. M.; Pohl, R. L. *J. Am. Chem. Soc.* **1966**, *88*, 5117–5121.
(21) Dessy, R. E.; Kornmann, R. L.; Smith, C.; Haytor, R. *J. Am. Chem. Soc.* **1968**, *90*, 2001–2004.
(22) Dessy, R. E.; Rheingold, A. L.; Howard, G. D. *J. Am. Chem. Soc.* **1972**, *94*, 746–752.
(23) Vahrenkamp, H. *Chem. Ber.* **1978**, *111*, 3472–3483.
(24) Ginsburg, R. E.; Rothrock, R. K.; Finke, R. G.; Collman, J. P.; Dahl, L. F. *J. Am. Chem. Soc.* **1979**, *101*, 6550–6562.
(25) Madach, T.; Vahrenkamp, H. *Chem. Ber.* **1981**, *114*, 513–526.
(26) Collman, J. P.; Rothrock, R. K.; Finke, R. G.; Moore, E. J.; Rose-Munch, F. *Inorg. Chem.* **1982**, *21*, 146–156.
(27) Darchen, A.; Mousser, H.; Patin, H. *J. Chem. Soc., Chem. Commun.* **1988**, 968–970.
(28) DiMaio, A. J.; Rheingold, A. L.; Chin, T. T.; Pierce, D. T.; Geiger, W. E. *Organometallics* **1998**, *17*, 1169–1176.
(29) Courtot-Coupez, J.; Guéguen, M.; Guerchais, J. E.; Pétillon, F. Y.; Talarmin, J.; Mercier, R. *J. Organomet. Chem.* **1986**, *312*, 81–95.
(30) El Khalifa, M.; Gueguen, M.; Mercier, R.; Petillon, F. Y.; Saillard, J. Y.; Talarmin, J. *Organometallics* **1989**, *8*, 140–148.
(31) Gueguen, M.; Petillon, F. Y.; Talarmin, J. *Organometallics* **1989**, *8*, 148–154.
(32) Windhager, J.; Rudolph, M.; Bräutigam, S.; Görls, H.; Weigand, W. *Eur. J. Inorg. Chem.* **2007**, 2748–2760.
(33) Capon, J.-F.; Ezzaher, S.; Gloaguen, F.; Petillon, F. Y.; Schollhammer, P.; Talarmin, J.; Davin, T. J.; McGrady, J. E.; Muir, K. W. *New J. Chem.* **2007**, *31*, 2052–2064.
(34) Teo, B. K.; Hall, M. B.; Fenske, R. F.; Dahl, L. F. *J. Organomet. Chem.* **1974**, *70*, 413–420.
(35) Teo, B. K.; Hall, M. B.; Fenske, R. F.; Dahl, L. F. *Inorg. Chem.* **1975**, *14*, 3103–3117.
(36) Burdett, J. K. *J. Chem. Soc., Dalton Trans.* **1977**, 423–428.
(37) Shaik, S.; Hoffmann, R. *J. Am. Chem. Soc.* **1980**, *102*, 1194–1196.
(38) Shaik, S.; Hoffmann, R.; Fisel, C. R.; Summerville, R. H. *J. Am. Chem. Soc.* **1980**, *102*, 4555–4572.
(39) Rizzi, G. A.; Granozzi, G.; Casarin, M.; Basato, M. *Organometallics* **1987**, *6*, 2536–2545.
(40) Reinhold, J.; Muller, B.; Eichler, U. *Organometallics* **1997**, *16*, 1497–1500.
(41) Palacios, A. A.; Aullon, G.; Alemany, P.; Alvarez, S. *Inorg. Chem.* **2000**, *39*, 3166–3175.
(42) Baik, M.-H.; Ziegler, T.; Schauer, C. K. *J. Am. Chem. Soc.* **2000**, *122*, 9143–9154.
(43) Baik, M.-H.; Schauer, C. K.; Ziegler, T. *J. Am. Chem. Soc.* **2002**, *124*, 11167–11181.
(44) Gennett, T.; Geiger, W. E.; Willett, B.; Anson, F. C. *J. Electroanal. Chem.* **1987**, *222*, 151–160.
(45) Baik, M.-H. *Density-functional-theory studies of molecules that undergo single two-electron redox reactions accompanied by structural changes*; University of North Carolina, Chapel Hill, NC, 2000.
(46) Baerends, E. J.; Gritsenko, O. V. *J. Phys. Chem. A* **1997**, *101*, 5383–5403.

against the experimentally observed redox potentials, these computer models reveal details of the electronic structure that are ultimately responsible for potential inversion. We examined the redox behavior of complexes **1**−**4** and present both a quantitative concept and a qualitative concept that explain the puzzling two-electron redox chemistry of these complexes.

Computational Details

Geometry optimizations and calculations of the thermochemical properties were carried out using DFT as implemented in the *Jaguar 7.0* suite of ab initio quantum chemistry programs.[47] Geometry optimizations were performed at the B3LYP/6-31G** level of theory with molybdenum and tungsten represented using the Los Alamos LACVP basis.[48−55] While this model chemistry generates reasonable structures, the energies are not reliable for redox phenomena, as was previously reported.[56] Subsequent single-point energy calculations were conducted with Dunning's correlation-consistent triple-ζ basis set, cc-pVTZ(-f),[57] with transition metals represented using a decontracted version of LACVP to match the effective core potential with a triple-ζ quality basis. Solvation energies were computed at the double-ζ level using a self-consistent-reaction-field approach based on numerical solutions of the Poisson−Boltzmann equation,[58,59] computed at the optimized gas phase geometry utilizing an appropriate dielectric constant for comparison to the experimental conditions ($\varepsilon = 37.5$ for acetonitrile; $\varepsilon = 20.7$ for acetone). The standard set of optimized radii in *Jaguar* was employed: Mo (1.526 Å), W (1.534 Å), P (2.074 Å), S (1.900 Å), H (1.150 Å), C (1.900 Å), and O (1.600 Å).[60] Vibrational analyses using analytical frequencies were also computed at the double-ζ level, ensuring that all stationary points were minima. Thermodynamic properties were obtained as summarized in eqs 5−8, with standard approximations assumed for the entropy corrections in the gas phase.[61] Solution phase free energies are obtained by adding the free energy of solvation to the gas phase free energy. Zero-point energies and entropy corrections were derived using unscaled frequencies.

Absolute potentials were converted to relative values versus Fc/Fc^+, utilizing values of 4.43 V for NHE and 0.548 V vs NHE for Fc/Fc^+.[62,63] In principle, one should both use the value of Fc/Fc^+ in the experimental solvent and account for the liquid junction potential in the electrochemical cell. The errors approximately cancel, however, and therefore our method gives practically useful results.[64] We have chosen to continue using our previously reported scheme for consistency.[56,65] Furthermore, the absolute potential for NHE is somewhat debated, with values ranging from 4.28 to 4.43 V,[62,66−70] and we acknowledge that systematic errors up to 150 mV may be present in our calculations by adopting the value of 4.43 V reported by Reiss and Heller.[62,70]

$$\Delta H(\text{gas}) = \Delta E(\text{SCF}) + \Delta\text{ZPE} \tag{5}$$

$$\Delta G(\text{gas}) = \Delta H(\text{gas}) - (298.15\ \text{K})\Delta S(\text{gas}) \tag{6}$$

$$\Delta G(\text{sol}) = \Delta G(\text{gas}) + \Delta\Delta G_{\text{solv}} \tag{7}$$

$$\Delta G^{\text{EA}}(\text{sol}) = -nFE^{\circ}_{\text{comp, abs}} \tag{8}$$

$$E^{\circ}_{\text{comp}} = E^{\circ}_{\text{comp, abs}} - 4.43^{62} - 0.548^{63} \tag{9}$$

ΔH(gas) = gas phase enthalpy change; ΔE(SCF) = electronic energy change; ΔZPE = zero-point energy correction difference; ΔG(gas) = gas phase Gibbs free energy change; ΔS(gas) = gas phase entropy change; ΔG(sol) = solution phase free energy change; $\Delta\Delta G_{\text{solv}}$ = free energy of solvation difference; ΔG^{EA}(sol) = solvated free energy change of reduction; $E^{\circ}_{\text{comp,abs}}$ = absolute standard reduction potential; E°_{comp} = standard reduction potential vs Fc/Fc^+.

Results and Discussion

Experimental Observations. We have previously presented electrochemical and spectroelectrochemical studies on several sulfido- and phosphido-bridged molydenum and tungsten complexes, which all exhibited two-electron redox chemistry.[16−19] Thermodynamic and kinetic parameters are summarized in Table 1. The following conclusions of these experimental studies are pertinent to this investigation. (i) Potential inversion occurs in both the $[M_2(\mu\text{-}SR)_2(CO)_8]^{0/2-}$ and $[M_2(\mu\text{-}PR_2)_2(CO)_8]^{0/2-}$ redox systems. Values of $\Delta E^{\circ\prime} = E^{\circ\prime}_{\text{ii}} - E^{\circ\prime}_{\text{i}}$ equal ca. +180 mV for the phosphido-bridged complexes and range from +20 to +230 mV for the sulfido-bridged complexes, depending on the experimental conditions. (ii) Values of $E^{\circ\prime}_{\text{i}}$, $E^{\circ\prime}_{\text{ii}}$, and $E^{\circ\prime}_{\text{obs}}$ are effectively metal-independent but are ∼0.5 V more negative for R_2P^-- versus RS^--bridged complexes, suggesting that the ligands may play a more important role than the metal centers. (iii) The results for $[Mo_2(\mu\text{-}PPh_2)_2(CO)_8]^{0/2-}$ and $[W_2(\mu\text{-}PPh_2)_2(CO)_8]^{0/2-}$ establish that the second electrode reaction is slower than the first ($k_{\text{sh,ii}} < k_{\text{sh,i}}$),[19] which is consistent with greater structural change accompanying the addition of the second electron. (iv) On the basis of these $k_{\text{sh,ii}}$ values, electron-transfer kinetics appear to be slightly faster for molybdenum than tungsten but are demonstrably greater for RS^- than R_2P^- complexes.

Structural Features. Our calculations reproduce the experimentally observed structures of the neutral and dianionic forms of complexes **1**−**4**, with the metal−metal and metal−ligand distances being overestimated by ca. 0.1 Å, as

(47) *Jaguar 7.0*; Schrödinger, LLC: New York, **2007**.
(48) Vosko, S. H.; Wilk, L.; Nusair, M. *Can. J. Phys.* **1980**, *58*, 1200–1211.
(49) Lee, C. T.; Yang, W. T.; Parr, R. G. *Phys. Rev. B* **1988**, *37*, 785–789.
(50) Becke, A. D. *Phys. Rev. A* **1988**, *38*, 3098–3100.
(51) Becke, A. D. *J. Chem. Phys.* **1993**, *98*, 5648–5652.
(52) Stephens, P. J.; Devlin, F. J.; Chabalowski, C. F.; Frisch, M. J. *J. Phys. Chem.* **1994**, *98*, 11623–11627.
(53) Hay, P. J.; Wadt, W. R. *J. Chem. Phys.* **1985**, *82*, 270–283.
(54) Hay, P. J.; Wadt, W. R. *J. Chem. Phys.* **1985**, *82*, 299–310.
(55) Wadt, W. R.; Hay, P. J. *J. Chem. Phys.* **1985**, *82*, 284–298.
(56) Baik, M.-H.; Friesner, R. A. *J. Phys. Chem. A* **2002**, *106*, 7407–7415.
(57) Dunning, T. H., Jr. *J. Chem. Phys.* **1989**, *90*, 1007–1023.
(58) Marten, B.; Kim, K.; Cortis, C.; Friesner, R. A.; Murphy, R. B.; Ringnalda, M. N.; Sitkoff, D.; Honig, B. *J. Phys. Chem.* **1996**, *100*, 11775–11788.
(59) Edinger, S. R.; Cortis, C.; Shenkin, P. S.; Friesner, R. A. *J. Phys. Chem. B* **1997**, *101*, 1190–1197.
(60) Rashin, A. A.; Honig, B. *J. Phys. Chem.* **1985**, *89*, 5588–5593.
(61) Cramer, C. J. *Essentials of computational chemistry: theories and models*., 2nd ed.; John Wiley: Hoboken, NJ, 2004.
(62) Reiss, H.; Heller, A. *J. Phys. Chem.* **1985**, *89*, 4207–4213.
(63) Bard, A. J.; Faulkner, L. R. *Electrochemical Methods*; John Wiley & Sons, Inc.: New York, 1980.
(64) Namazian, M.; Coote, M. L. *J. Phys. Chem. A* **2007**, *111*, 7227–7232.
(65) Lord, R. L.; Schultz, F. A.; Baik, M.-H. *J. Am. Chem. Soc.* **2009**, *131*, 6189–6197.
(66) Tissandier, M. D.; Cowen, K. A.; Feng, W. Y.; Gundlach, E.; Cohen, M. H.; Earhart, A. D.; Coe, J. V.; Tuttle, T. R. *J. Phys. Chem. A* **1998**, *102*, 7787–7794.
(67) Tissandier, M. D.; Cowen, K. A.; Feng, W. Y.; Gundlach, E.; Cohen, M. H.; Earhart, A. D.; Tuttle, T. R.; Coe, J. V. *J. Phys. Chem. A* **1998**, *102*, 9308–9308.
(68) Zhan, C.-G.; Dixon, D. A. *J. Phys. Chem. A* **2001**, *105*, 11534–11540.
(69) Kelly, C. P.; Cramer, C. J.; Truhlar, D. G. *J. Phys. Chem. B* **2006**, *110*, 16066–16081.
(70) Fawcett, W. R. *Langmuir* **2008**, *24*, 9868–9875.

Table 1. Thermodynamic and Kinetic Parameters for $[M_2(\mu\text{-}L)_2(CO)_8]^{0/2-}$ Redox Couples

M_2L_2	solvent, electrolyte	$E^{\circ\prime}_{obs}$,[a] V	$E^{\circ\prime}_{calc}$,[b] V	$E^{\circ\prime}_{i}$, V	$E^{\circ\prime}_{ii}$, V	$\Delta E^{\circ\prime}$, mV	$k_{sh,i}$, cm s^{-1}	$k_{sh,ii}$, cm s^{-1}	ref
$Mo_2(SPh)_2$	CH_3CN, 0.1 M $TBABF_4$	−0.80							16
$Mo_2(PPh_2)_2$	acetone, 0.3 M $TBAPF_6$	−1.36	−1.37	−1.45	−1.28	170	0.4	0.038	19
$W_2(SPh)_2$	CH_3CN, 0.1 M $TBABF_4$	−0.82							16
$W_2(PPh_2)_2$	acetone, 0.3 M $TBAPF_6$	−1.32	−1.35	−1.44	−1.26	180	0.8	0.014	19
$W_2(SBz)_2$	DMF, 0.1 M $TBABF_4$	−0.95	−0.94	−0.95	−0.93	20	≥0.1	≥0.1	17
$W_2(SBz)_2$	CH_2Cl_2, 0.1 M $TBAPF_6$	−1.07	−1.08	−1.19	−0.96	230			18

[a] Measured as $(E_{pa} + E_{pc})/2$ by cyclic voltammetry, where E_{pa} and E_{pc} are the anodic and cathodic peak potentials. [b] Calculated as $(E^{\circ\prime}_{i} + E^{\circ\prime}_{ii})/2$ following analysis of the two-electron behavior.

Table 2. Redox Induced Differences in the Structure for $[M_2(\mu\text{-}L)_2(CO)_8]^{0/-/2-}$ [a]

	$Mo_2(\mu\text{-}PPh_2)_2$ (**1**)			$W_2(\mu\text{-}PPh_2)_2$ (**2**)		
	$\mathbf{1}^-/\mathbf{1}^0$	$\mathbf{1}^{2-}/\mathbf{1}^-$	$\mathbf{1}^{2-}/\mathbf{1}^0$	$\mathbf{2}^-/\mathbf{2}^0$	$\mathbf{2}^{2-}/\mathbf{2}^-$	$\mathbf{2}^{2-}/\mathbf{2}^0$
ΔM−M	0.482	0.632	1.114 (1.060)	0.499	0.599	1.098 (1.076)
ΔM−L	0.069	0.069	0.138 (0.132)	0.051	0.071	0.121 (0.118)
ΔL−L	−0.237	−0.496	−0.733 (−0.683)	−0.305	−0.460	−0.765 (−0.740)
ΔM−L−M	11.6	17.2	28.8 (27.8)	12.9	16.3	29.2 (29.1)
ΔL−M−L	−11.7	−17.1	−28.8 (−27.8)	−13.0	−16.2	−29.2 (−29.3)
Δ$M-CO_{ax}$	−0.008	−0.003	−0.012 (−0.015)	−0.007	−0.003	−0.010 (−0.037)
Δ$M-CO_{eq}$	−0.024	−0.024	−0.048 (−0.091)	−0.020	−0.025	−0.046 (−0.062)
Δ$C-O_{ax}$	0.005	0.005	0.011 (0.006)	0.006	0.005	0.011 (0.004)
Δ$C-O_{eq}$	0.009	0.012	0.021 (0.050)	0.011	0.013	0.023 (0.028)
	$Mo_2(\mu\text{-}SPh)_2$ (**3**)			$W_2(\mu\text{-}SPh)_2$ (**4**)		
	$\mathbf{3}^-/\mathbf{3}^0$	$\mathbf{3}^{2-}/\mathbf{3}^-$	$\mathbf{3}^{2-}/\mathbf{3}^0$	$\mathbf{4}^-/\mathbf{4}^0$	$\mathbf{4}^{2-}/\mathbf{4}^-$	$\mathbf{4}^{2-}/\mathbf{4}^0$
ΔM−M	0.434	0.780	1.214 (1.105)	0.451	0.706	1.157 (1.087)
ΔM−L	0.088	0.077	0.165 (0.134)	0.071	0.062	0.133 (0.113)
ΔL−L	−0.126	−0.606	−0.732 (−0.699)	−0.187	−0.576	−0.763 (−0.742)
ΔM−L−M	9.2	21.0	30.2 (28.9)	10.4	19.6	30.0 (29.4)
ΔL−M−L	−9.2	−20.9	−30.1 (−28.9)	−10.4	−19.6	−30.0 (−29.4)
Δ$M-CO_{ax}$	−0.008	−0.005	−0.013 (−0.013)	−0.008	−0.004	−0.012 (−0.011)
Δ$M-CO_{eq}$	−0.044	−0.032	−0.075 (−0.086)	−0.039	−0.028	−0.067 (−0.080)
Δ$C-O_{ax}$	0.005	0.006	0.011 (−0.027)	0.005	0.006	0.012 (−0.016)
Δ$C-O_{eq}$	0.013	0.012	0.025 (0.028)	0.013	0.013	0.025 (0.050)

[a] Experimental values for the overall two-electron process are given in parentheses. Bond lengths are in angstroms and angles are in degrees.

is commonly observed in DFT calculations for transition-metal complexes.[61] Selected bond lengths and bond angles of the calculated structures are compared with crystal structure data[71−78] in Table S1 (Supporting Information). A summary of calculated structural *differences* accompanying the first (eq 1), second (eq 2), and overall two-electron (eq 4) reductions of the four compounds is presented in Table 2, and a pictorial representation of the induced structural changes is presented in Figure 2 for complex **3**. Several key elements of the structural change attending two-electron transfer in **1**−**4** are apparent. Although M−M distances and M−L−M angles increase by 1.1−1.2 Å and 20−30°, respectively, and L−L distances and L−M−L angles decrease by 0.7−0.8 Å and 20−30° upon overall two-electron reduction, these nuclear reorganizations are not distributed equally between the two electron-transfer steps. More than half the change in these parameters (55−83%) accompanies the addition of the second electron, while changes in the metal-bridging ligand distance (ΔM−L = 0.05−0.09 Å) are more evenly divided between the two redox steps. The asymmetry in the amount of structural change is consistent with the heterogeneous rate constants being smaller for the second electron transfer because of larger inner-shell reorganization. For the carbonyl ligands, both M−C and C−O bond lengths are influenced significantly by electron transfer; the former metric decreases while the latter increases upon reduction, reporting on an increase in the metal−CO π-backbonding. Differences in the back-bonding for equatorial and axial COs reflect the fact that the redox-active molecular orbital (LUMO in neutral species and HOMO in dianion species) is delocalized into the equatorial carbonyl π^* orbitals coplanar with the M_2L_2 diamond core (vide infra).[19,37,41]

Redox Potentials and Disproportionation Free Energies. The thermodynamics of the electron-transfer reactions for **1**−**4** were evaluated using the method previously described.[56] Table 3 enumerates one- and two-electron redox potentials referenced against Fc/Fc^+ (E°_{comp}) as well as the disproportionation free energy for **1**−**4**, with comparisons to experimental values ($E^{\circ\prime}_{obs}$) where possible.

(71) Shyu, S. G.; Calligaris, M.; Nardin, G.; Wojcicki, A. *J. Am. Chem. Soc.* **1987**, *109*, 3617–3625.
(72) Darensbourg, D. J.; Sanchez, K. M.; Reibenspies, J. *Inorg. Chem.* **1988**, *27*, 3636–3643.
(73) Zhuang, B.; Huang, L.; He, L.; Yang, Y.; Lu, J. *Inorg. Chim. Acta* **1989**, *157*, 85–90.
(74) Wong, W.-T.; Wong, W.-K. *Acta Crystallogr., Sect. C* **1994**, *50*, 1404–1406.
(75) Zhuang, B.; Huang, L.; He, L. *Jiegou Huaxue* (*Chin. J. Struct. Chem.*) **1995**, *14*, 359.
(76) Maitra, K.; Catalano, V. J.; Nelson, J. H. *J. Organomet. Chem.* **1997**, *529*, 409–422.
(77) Zhuang, B.; Sun, H.; Pan, G.; He, L.; Wei, Q.; Zhou, Z.; Peng, S.; Wu, K. *J. Organomet. Chem.* **2001**, *640*, 127–139.
(78) Planinic, P.; Matkovic-Calogovic, D. *Struct. Chem.* **2001**, *12*, 439–444.

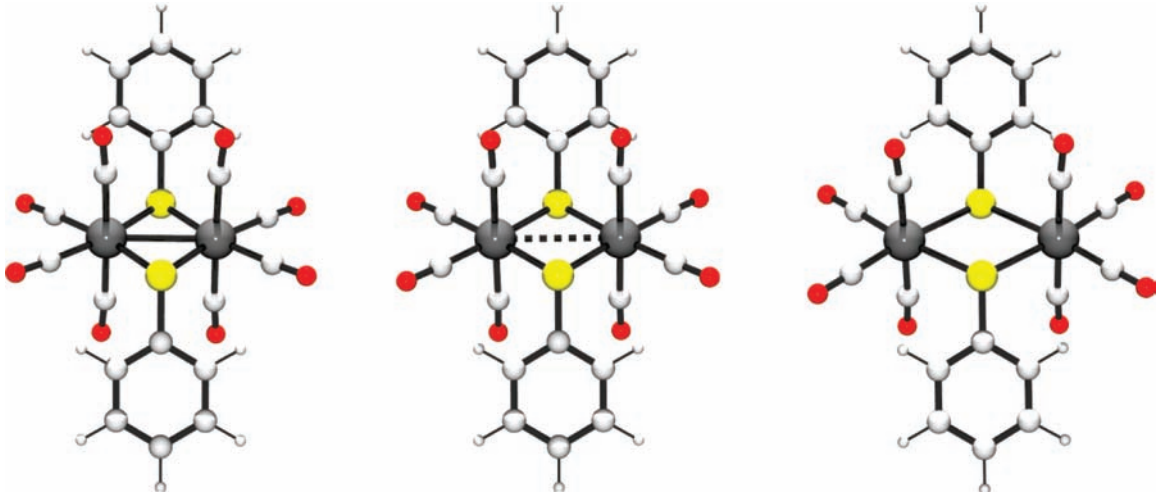

Figure 2. Example of the geometry changes upon two-electron reduction for $Mo_2(\mu\text{-}SPh)_2(CO)_8$.

Table 3. Summary of the Thermodynamics for Electron Transfer and Disproportionation for **1**−**4**

reaction	ΔG(gas), eV	$\Delta\Delta G_{solv}$, eV	ΔG(sol), eV	$E°_{comp}$, V vs Fc/Fc^+	$E°'_{obs}$, V vs Fc/Fc^+
$\mathbf{1}^0 + e^- \rightarrow \mathbf{1}^-$	−2.276	−1.288	−3.564	−1.414	
$\mathbf{1}^- + e^- \rightarrow \mathbf{1}^{2-}$	0.148	−3.687	−3.539	−1.439	
$\mathbf{1}^0 + 2e^- \rightarrow \mathbf{1}^{2-}$	−2.128	−4.975	−7.103	**−1.427**	**−1.36**
$2\,\mathbf{1}^- \rightarrow \mathbf{1}^0 + \mathbf{1}^{2-}$	2.424	−2.398	0.025	**−0.025**	
$\mathbf{2}^0 + e^- \rightarrow \mathbf{2}^-$	−2.222	−1.301	−3.523	−1.455	
$\mathbf{2}^- + e^- \rightarrow \mathbf{2}^{2-}$	0.046	−3.727	−3.681	−1.297	
$\mathbf{2}^0 + 2e^- \rightarrow \mathbf{2}^{2-}$	−2.177	−5.028	−7.204	**−1.376**	**−1.32**
$2\,\mathbf{2}^- \rightarrow \mathbf{2}^0 + \mathbf{2}^{2-}$	2.268	−2.426	−0.158	**0.158**	
$\mathbf{3}^0 + e^- \rightarrow \mathbf{3}^-$	−2.997	−1.352	−4.348	−0.630	
$\mathbf{3}^- + e^- \rightarrow \mathbf{3}^{2-}$	−0.292	−4.048	−4.340	−0.638	
$\mathbf{3}^0 + 2e^- \rightarrow \mathbf{3}^{2-}$	−3.288	−5.400	−8.688	**−0.634**	**−0.80**
$2\,\mathbf{3}^- \rightarrow \mathbf{3}^0 + \mathbf{3}^{2-}$	2.705	−2.697	0.008	**−0.008**	
$\mathbf{4}^0 + e^- \rightarrow \mathbf{4}^-$	−2.968	−1.359	−4.327	−0.651	
$\mathbf{4}^- + e^- \rightarrow \mathbf{4}^{2-}$	−0.278	−4.072	−4.349	−0.629	
$\mathbf{4}^0 + 2e^- \rightarrow \mathbf{4}^{2-}$	−3.246	−5.430	−8.676	**−0.640**	**−0.82**
$2\,\mathbf{4}^- \rightarrow \mathbf{4}^0 + \mathbf{4}^{2-}$	2.691	−2.713	−0.023	**0.023**	

A detailed breakdown of these free energy changes in terms of their fundamental components (see eqs 5−8) is given in the Supporting Information (Table S2). Table 3 focuses on the gas phase electron attachment energy ΔG(gas), differential solvation energy $\Delta\Delta G_{solv}$, solution phase free energy ΔG(sol), and the corresponding potentials $E°_{comp}$. To model the different solvents used during the voltammetric experiments, dielectric values (ε) of 20.7 and 37.5 were assumed for acetone (**1** and **2**) and acetonitrile (**3** and **4**), respectively, and all potentials (experimental and computed) have been referenced against Fc/Fc^+. While the one-electron reduction potentials are listed in Table 3 for completeness, the two-electron potentials (eq 4) and disproportionation thermodynamics (eq 3) are more directly comparable to experiment.

In all four cases, our calculations suggest that the first and second redox potentials are remarkably close in energy. For **2** and **4**, we reproduce the experimentally observed potential inversion, with the former being inverted by 158 mV and the latter by 23 mV. Our calculations place the second reduction more negative than the first by 25 and 8 mV for complexes **1** and **3**, respectively; i.e., the potential inversion is not predicted. It is important to avoid overinterpretation of these results in terms of their precision. Within the errors of our model, we predict the apparent two-electron transfer, or two irresolvable one-electron events, for all species. The extent of potential inversion was not experimentally measured for **3** and **4** because of facile electron-transfer kinetics and competing solvolysis pathways, but related systems bridged by SBz^- exhibit solvent-dependent potential inversion between 20 and 230 mV. Potential inversions of 170 and 180 mV were observed for the molybdenum and tungsten phosphido-bridged dimers, which differs from the computed result for molybdenum (−25 mV) but agrees quite well for tungsten (158 mV). Thus, our model chemistry appears to reproduce both the asymmetry in the amount of structural change per reduction step and the correlated thermodynamics that are observed experimentally reasonably well. We also compared the average of the two single-electron potentials with the experimentally observed two-electron redox potentials. Redox potentials for the phosphido-bridged species are computed as −1.427 and −1.376 V for **1** and **2**, respectively, comparing favorably with the experimental values of −1.36 and −1.32 V. A larger discrepancy is seen between the computed values of −0.634 and −0.640 V versus experimental values of −0.80 and −0.82 V for the sulfido-bridged complexes. Despite the slight discrepancy, our calculations capture the key components of the redox series of interest.

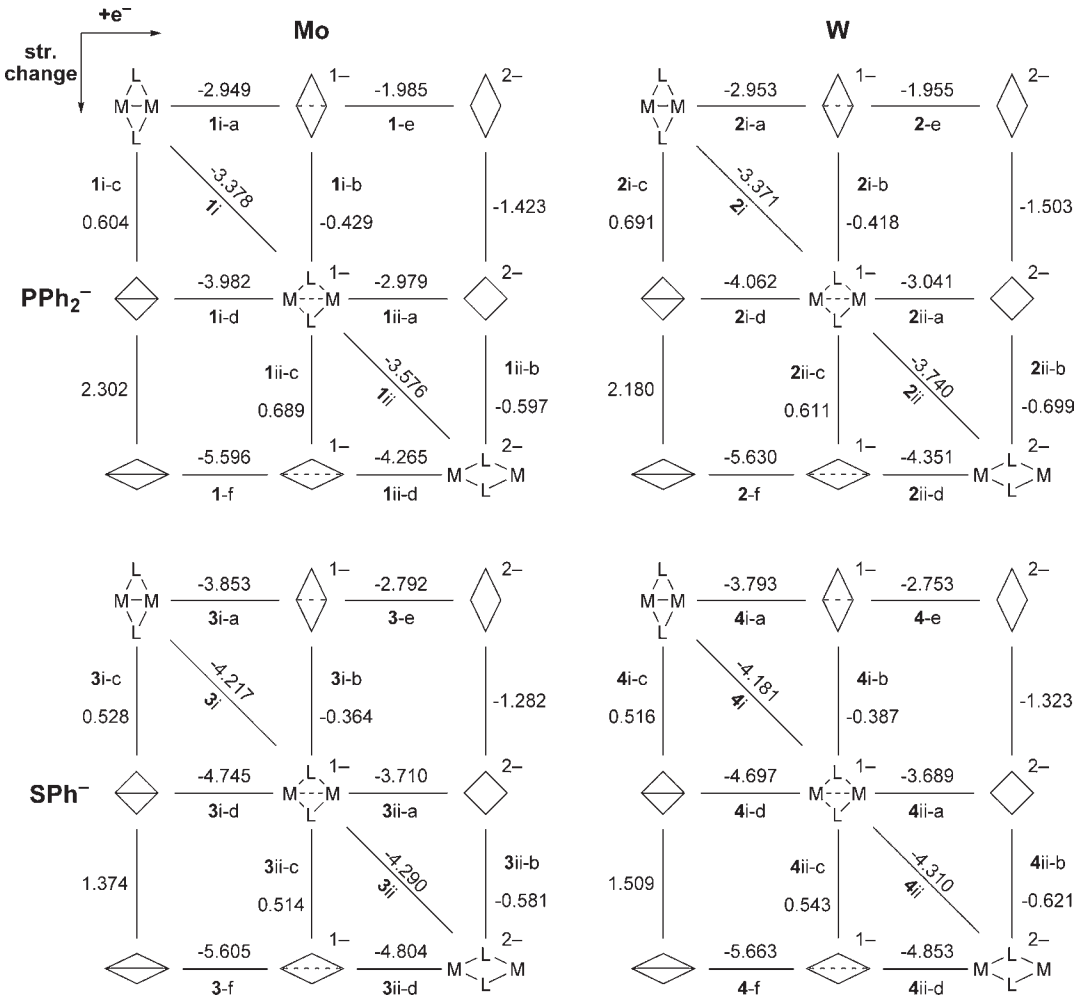

Figure 3. Theoretical square schemes decoupling vertical electron-transfer events (horizontal direction) from the accompanying structural change (vertical direction) for **1**−**4**. $\Delta G(\mathrm{sol})'$ values are listed in electronvolts.

With these data in hand, we can investigate the mechanism by which the potentials for these compounds come so close to one another. Because solvation energies increase significantly with charge, we cannot expect gas phase energies to give meaningful trends, as seen by the gas phase free energies in Table 3. Given that the process of interest traverses the charge states $0 \rightarrow 1- \rightarrow 2-$, one plausible source of the disproportionate energy change is solvation energy because we may expect the dianion to be much more strongly solvated than the monoanion. Examining the $\Delta\Delta G_{\mathrm{solv}}$ components for the two steps, however, we find that the differential solvation energy of the second reduction is less than expected based on a simple Born model analysis ($\Delta\Delta G_{\mathrm{solv\text{-}ii}} < 2^2\Delta\Delta G_{\mathrm{solv\text{-}i}}$) throughout the series. Why then are the two reduction potentials for the complexes **1**−**4** so close? To address this question, we made use of an energy-partitioning protocol previously used to analyze similar systems.[43]

Theoretical Square Schemes. As illustrated in Figure 3, a series of calculations were carried out to partition the reduction energies by considering electron transfer and structural rearrangement steps separately. Along the horizontal lines of the diagrams, we disallow structural change while adding electrons sequentially. The energy differences indicated on the lines that connect these isostructural species are vertical electron attachment energies. We change the structure while maintaining the electron count vertically and thereby quantify structural reorganization energies. Because this diagram is reminiscent of square diagrams that are often used in electrochemistry, we call it a *theoretical square scheme*. By construction, the off-diagonal states are not minima on their respective potential energy surfaces and the harmonic approximation used to derive zero-point energies and entropic contributions is no longer valid. Consequently, we introduce a new approximate free energy, $\Delta G(\mathrm{sol})' = \Delta E(\mathrm{SCF}) + \Delta\Delta G_{\mathrm{solv}}$. Figure 3 summarizes $\Delta G(\mathrm{sol})'$ values for **1**−**4**. The most relevant steps are labeled for ease of reference.[79]

As was observed for the true free energies, $\Delta G(\mathrm{sol})'_{\mathrm{ii}}$ and $\Delta G(\mathrm{sol})'_{\mathrm{i}}$ are largely dependent on the bridging ligand and not the metal identity, which may be surprising because the metal centers are commonly thought to dominate the chemical properties of a complex. Potentials

(79) Starting with the oxidized species for a given square, it is natural to view reduction partitioned into vertical electron attachment (step a) followed by structural relaxation (step b), which takes place on the upper triangle of the square. The lower triangle involves a spontaneous structural deformation that is well-defined numerically but lacks physical motivation. Conversely, if we start with the reduced species (bottom right corner of i or ii), the lower triangle now becomes most meaningful by viewing oxidation as vertical ionization (step d) followed by structural relaxation (step c). All energy differences are referenced from left to right and from top to bottom.

computed using $\Delta G(\mathrm{sol})'$ are 50−90 mV more negative than those from Table 3,[80] but are still in good agreement with the experimental values. Unlike $\Delta G(\mathrm{sol})$, $\Delta G(\mathrm{sol})'$ predicts the second electron transfer to be more favorable for every system, as evidenced by disproportionation energies ($\Delta\Delta G(\mathrm{sol})'_{\mathrm{disp}} = \Delta G(\mathrm{sol})'_{\mathrm{ii}} - \Delta G(\mathrm{sol})'_{\mathrm{i}}$) of −0.198, −0.369, −0.073, and −0.139 eV for **1**−**4**, respectively. In the absence of structural relaxation, the second reduction is disfavored by 0.8−1.3 V, as illustrated along the rows in the square diagram regardless of which row is considered (e/i-a for neutrals, ii-a/i-d for anions, or ii-d/f for dianions). Thus, if structural changes are ignored, all systems would demonstrate normal potential ordering. Closer examination of the adiabatic reduction steps i and ii is enlightening. In the $MoPPh_2$ system **1**, the vertical electron attachment to the monoanionic species, step **1**ii-a, is favored over that to the neutral species by 0.030 eV (step **1**i-a). Similarly, species **2** also exhibits this unusual behavior with potentials of −3.041 and −2.953 eV, respectively, to afford an inversion of 88 mV. In the sulfido-bridged analogues **3** and **4**, normal ordering (i-a < ii-a) is seen with an energy difference of 0.143 and 0.104 eV in favor of the first step. In contrast to the vertical electron attachment energies, differential structural relaxations computed as $\Delta G(\mathrm{sol})'_{\mathrm{ii\text{-}b}} - \Delta G(\mathrm{sol})'_{\mathrm{i\text{-}b}}$ favor the second reduction for all four systems by 0.168, 0.281, 0.217, and 0.234 eV for **1**−**4**, respectively, an outcome that ensures potential inversion in the case of **1** and **2** and makes it feasible or nearly so in the case of **3** and **4**. This observation is important. One expects the differential electron attachment energy to dominate the energetics ($|\Delta\Delta G(\mathrm{sol})'_{\mathrm{a}}| > |\Delta\Delta G(\mathrm{sol})'_{\mathrm{b}}|$) of the electron transfer because the accompanying absolute energies, $\Delta G(\mathrm{sol})'_{\mathrm{a}}$, are much larger than those associated with the structural change, $\Delta G(\mathrm{sol})'_{\mathrm{b}}$. Because we see the inverse situation, $|\Delta\Delta G(\mathrm{sol})'_{\mathrm{a}}| < |\Delta\Delta G(\mathrm{sol})'_{\mathrm{b}}|$, there must be a feature that we have not yet identified that brings the two vertical attachment energies unusually close in energy. Thus, identifying the electronic structure features responsible for $\Delta\Delta G(\mathrm{sol})'_{\mathrm{a}}$ being so small is critical to understanding what drives the apparent two-electron behavior in these ligand-bridged systems.

One major difference between the PPh_2^- and SPh^- ligands is that the phosphido ligand enforces a much more compact M_2L_2 core to accommodate the steric demand of the second phenyl unit while shielding the core more effectively from solvent access. As a consequence, we expect that the Coulombic penalty of adding a second electron to the dinuclear core should be more pronounced in the PPh_2^--bridged system compared to the SPh^--bridged analogue. Similarly, the greater solvent accessibility of the charge should give rise to a more dramatic solvation energy difference in the sulfido complex, as electrons are added sequentially. The solvation energy difference for the vertical electron attachments is indeed more pronounced in **3** and **4** as compared to **1** and **2** (Table 4), distorting the overall energy by ∼350 meV more toward the fully reduced dianionic species and thus favoring potential inversion. In contrast and against our expectation, the electronic driving force is ∼550 meV less positive for **1** and **2**, which reflects on a smaller Coulombic penalty that **1** and **2** must pay to accommodate the second electron. Ultimately, these two important features combine to result in all species having unusually small $|\Delta\Delta G(\mathrm{sol})'_{\mathrm{a}}|$ values, but the electronic structure distortions for **1** and **2** are more dramatic than those for **3** and **4**. This insight is interesting because it is easier to design rationally electronic features that redistribute charge than to control how the charge is exposed to solvents. Thus, from the perspectives of future design strategies, the phosphido ligands provide an advantage over the sulfido analogues.

(80) Computed with $\Delta G(\mathrm{sol})'$: E° = −1.501, −1.422, −0.724, and −0.732 V for **1**−**4**, respectively.

Table 4. Decomposition of $\Delta\Delta G(\mathrm{sol})'_{\mathrm{a}}$ Values for **1**−**4**[a]

species	$\Delta\Delta E(\mathrm{SCF})_{\mathrm{a}}$	$\Delta\Delta\Delta G_{\mathrm{solv,a}}$	$\Delta\Delta G(\mathrm{sol})'_{\mathrm{a}}$
1	+2.425	−2.455	−0.030
2	+2.401	−2.488	−0.087
3	+2.973	−2.830	+0.143
4	+2.945	−2.840	+0.105

[a] All values are reported in electronvolts.

Orbital Rationale for Potential Inversion

Whereas the above analysis gives an intuitively understandable comparison of the different energy components between the phosphido- and sulfido-bridged systems, it is still unclear why the second electron can be added with relative ease in both systems. Figure 4 shows the most relevant molecular orbitals for the molybdenum compounds **1** and **3**. We limit our discussion to these species because the tungsten-containing analogues **2** and **4** display essentially identical behavior compared to their molybdenum counterparts. Analogous plots for **2** and **4** are given in the Supporting Information. In addition to the redox-active orbital, a lower lying orbital is tracked (vide infra). Five states are presented for each species A: the neutral (A^0), monoanionic (A^-), and dianionic (A^{2-}) species, as well as the intermediate electronic structures at the constrained geometries ($A^{*,-}$ and $A^{*,2-}$) that were introduced in the square scheme. Vertical electron attachment steps Ai-a and Aii-a correspond to $A^0 \rightarrow A^{*,-}$ and $A^- \rightarrow A^{*,2-}$, respectively, while relaxation steps for the first and second reductions (Ai-b and Aii-b) correlate with $A^{*,-} \rightarrow A^-$ and $A^{*,2-} \rightarrow A^{2-}$. For monoreduced, odd-electron species, the average of the α and β orbital energies is reported for simplicity because of our use of an unrestricted formalism. Absolute orbital energies increase by 2−3 eV for each additional electron on average. To preserve the energy scale during the vertical electron attachments, we have identified the valence orbital that feels the least electrostatic repulsion to define a background Coulombic impact. This orbital is a π orbital of the bridging group phenyl moiety in each case and surprisingly changes by approximately the same amount for each electron transfer (+2.644/+2.583 and +2.803/+2.742 eV for **1**i-a/**1**ii-a and **3**i-a/**3**ii-a, respectively) despite different overall charges of the complexes. Background energy adjustments are not necessary for the structural relaxation steps.

The redox-active orbital was originally envisioned to be metal−metal σ antibonding between the $d_{x^2-y^2}$ orbital on each molybdenum center, with some in-plane CO backbonding participation. As can be seen in the orbital plots, however, the bridging P/S p orbitals contribute significantly to the redox-active orbital, especially in the oxidized states. While somewhat surprising, this finding nicely explains the anecdotal observation that the redox potentials are more dependent on the bridging ligand than the nature of the metal. More accurately, we may describe the redox-active orbital as the out-of-phase combination of two fragment orbitals: the metal−metal σ^* orbital on $[M_2(CO)_8]^{n+}$ (n = 2,

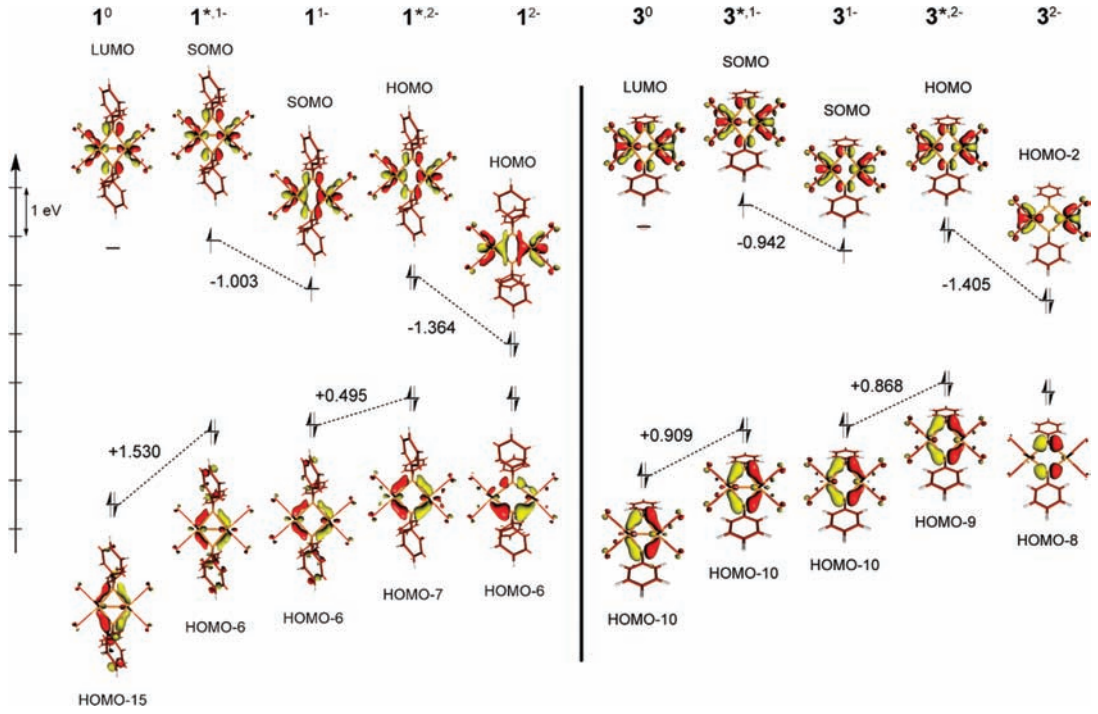

Figure 4. Isosurface plots (0.05 au) and relative energies (eV) of the redox-active orbital and its in-phase counterpart as a function of the redox state and structure for the Mo/PPh_2^- (**1**) and Mo/SPh^- (**3**) systems. Orbital energy changes upon electron addition (i.e., $\mathbf{1}^0 \rightarrow \mathbf{1}^{*,-}$) and structural relaxation (i.e., $\mathbf{1}^{*,-} \rightarrow \mathbf{1}^-$) are quantified where significant.

1, 0) and the $[L_2]^{2-}$ p−π orbital. Thus, both bonding and antibonding combinations of these fragment orbitals are shown for each of the states in Figure 4.

For both **1** and **3**, the relative destabilization that the redox-active orbitals experience is *larger* for the first electron attachment than it is for the second by 1.030 eV (**1**i-a: +1.699 eV; **1**ii-a: +0.669 eV) and 0.038 eV (**3**i-a: +1.347 eV; **3**ii-a: +1.308 eV), respectively, as highlighted in Figure 4. Most of these differences are traced to orbital energy changes for the in-phase complement of the redox-active orbital. Inserting the first electron into $\mathbf{1}^0$ and thus occupying the LUMO increases the energy of HOMO−15, the in-phase complement of the LUMO, by 1.530 eV. Injection of the second electron into the SOMO of $\mathbf{1}^-$ destabilizes the same orbital, which has become HOMO−6, by a relatively modest 0.495 eV. Similarly, the response of HOMO−10 in $\mathbf{3}^0$ to the first reduction is notably greater, with 0.909 eV compared to 0.868 eV in $\mathbf{3}^-$, although much less so than in the former complex. As expected, the structural relaxations $\mathbf{1}^{*,-} \rightarrow \mathbf{1}^-$, $\mathbf{1}^{*,2-} \rightarrow \mathbf{1}^{2-}$, $\mathbf{3}^{*,-} \rightarrow \mathbf{3}^-$ and $\mathbf{3}^{*,2-} \rightarrow \mathbf{3}^{2-}$ affect the SOMO and HOMO energies most because the structural relaxation provides relief to the electronic stress caused by the metal−metal antibonding interaction. Whereas this selected orbital energy evolution is only one part of the overall electronic energy, it captures the most important character of the redox-triggered structural change.

The spatial relationship of the in-phase and out-of-phase orbitals explains much about the observed electrostatics. For neutral species $\mathbf{1}^0$, contributions from both the metal and bridging ligand fragments are approximately equal in both the in-phase (HOMO−15) and out-of-phase (LUMO) combinations. As illustrated in the isosurface plots in Figure 4, both orbitals are fully delocalized among the constituents of the M_2L_2 core, and while the phases of the fragment orbitals are different, both orbitals are spatially very similar to each other.

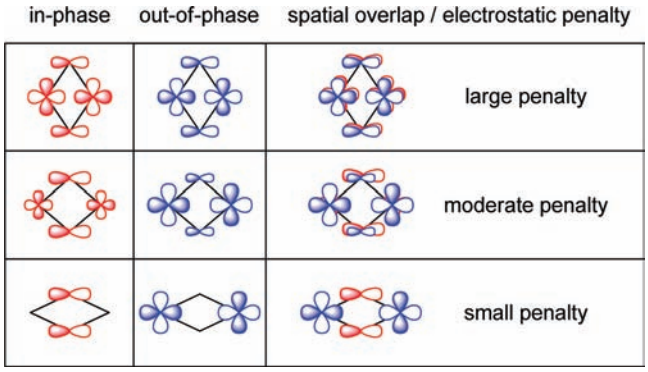

Figure 5. Cartoon demonstrating the spatial overlap between the in-phase (red) and out-of-phase (blue) orbitals relating to the redox behavior that gives rise to the disproportionate electrostatic penalty.

Occupation of the LUMO by one electron results in a large electrostatic penalty for the in-phase orbital because of this spatial similarity, as emphasized by the cartoons in Figure 5 (top, large penalty). After structural relaxation to $\mathbf{1}^-$, the SOMO is more metal-based in character and becomes spatially confined to a great extent along the M−M vector, whereas the in-phase orbital (HOMO−6) is mostly localized along the edges of the diamond core (Figure 5, middle, moderate penalty). Thus, the electrostatic cost is not expected to be as large because of the smaller spatial overlap between the electrons in these two orbitals, and this is indeed the case for **1**ii-a compared **1**i-a (0.495 vs 1.530 eV). This effect is maximized when the second electron is added because the structural relaxation leads to further spatial separation of the two molecular orbitals on the M_2 and L_2 units, respectively, as illustrated in Figures 4 and 5. In the dianionic complex, the metal−metal σ^* orbital and the lone-pair orbitals on the bridging ligands no longer communicate, which, in turn, allows for an

energetically more favorable accommodation of the second electron. Overall, this relatively intuitive electronic structure change leads to the differential electron attachment energy that is required for redox potential inversion. This principle can be recognized in the HOMO−6/HOMO pair of $\mathbf{1}^{2-}$ illustrated in Figure 4, where HOMO−6 has essentially become a purely phosphorus-based molecular orbital, while the HOMO is mostly metal-based. The corresponding orbital pair, HOMO−15/LUMO, in $\mathbf{1}^{0}$ has a substantially larger overlap, as shown in the top cartoon of Figure 5. The same trends are also seen in the HOMO−10/LUMO and HOMO−8/HOMO−2 pairs in $\mathbf{3}^{0}$ and $\mathbf{3}^{2-}$, respectively. This electronic feature is ultimately responsible for affording the smaller electronic driving force difference of +2.425 vs +2.973 eV for $\Delta\Delta E(\mathrm{SCF})_a$ reported in Table 4 and brings the differential electronic energy into a range, where the intrinsically larger solvation energy of the second step 1− → 2− compared to 0 → 1− cancels the electronic energy difference, to give a thermodynamic scenario that allows for potential inversion.

Why are the sulfido-bridged systems so different in how the electronic and solvation energies are distributed compared to the phosphido system (Table 4)? Extensive mixing between the metal and bridging ligand orbitals is present in the sulfido-bridged $\mathbf{3}^{0}$ as well, but the higher electronegativity of sulfur compared to phosphorus results in lower orbital energies for $[\mathrm{SPh}^{-}]_2$ and, hence, less equal weighting of the ligand-based fragment orbitals in the molecular orbitals. Stated differently, the sulfido bridges are more redox innocent than the phosphido ligands in this instance because of the overall charge of the metal carbonyl fragment. This slight, yet distinctive, difference from the phosphido-bridged system is most apparent in the ligand-dominated in-phase orbital of $\mathbf{3}^{0}$ (HOMO−10) and $\mathbf{3}^{-}$ (HOMO−10): Because (i) the orbital matching is not as efficient and (ii) there is more carbonyl backbonding character, the electronic structure in the diamond core changes less dramatically from $\mathbf{3}^{0}$ to $\mathbf{3}^{-}$ and results in approximately equal electrostatic penalties for the in-phase orbitals for both **3**i-a and **3**ii-a (+0.909 and +0.868 eV). The absolute value for these penalties is intermediate between the electrostatic penalties paid by the in-phase orbital of **1** (+1.530 and +0.495 eV), indicating that it falls between the large and moderate penalty scenarios of Figure 5.

Conclusions

Utilizing a methodology previously established by one of us, we have analyzed the title compounds to improve our understanding and pinpoint which molecular feature gives rise to their redox potential inversion. Gratifyingly, we were able to confirm the hypothesized larger structural change attending the second electron reduction responsible for more sluggish electron-transfer kinetics, as well as the reported thermodynamics including absolute potentials and observation of potential inversion.

Theoretical square schemes allowed for dissection of the free energies for the reductions into vertical electron attachment energies and structural relaxation steps. Generally, electron attachment energies are substantially larger than those associated with structural changes: a fundamental point that is often not recognized in the treatment of structural change within electrochemical systems (i.e., within a simple harmonic oscillator treatment of Marcus theory). The structural change was found to drive redox potential inversion, which is remarkable when we consider that the structural relaxation energies are approximately one-sixth of the electron attachment energies. Thus, we turned to an electronic structure analysis of the vertical attachment steps to determine why these values are so similar.

Both compounds demonstrated a significant amount of bridging ligand character in the redox-active orbitals. The extent of ligand participation is remarkably large, which is interesting because our bridging ligands are not involved in any aromatic delocalization and the electronic flexibility is in the σ subspace rather than the π subspace. A lower electron affinity of the phosphido group allowed for more extensive communication with the metals and thus a larger electronic bias for potential inversion. Despite the larger predisposition of **1** and **2** toward potential inversion due to electronics, the amount of potential inversion in both classes of molecules studied here was found to be approximately equal because of the open diamond cores of **3** and **4**, allowing for more solvation energy compensation.

The critical importance of orbital energy matching between fragments suggests one possible way that potential inversion can be rationally tuned in similar d^5, $d^5 + 2e^- \rightarrow d^6$, d^6 diamond-core systems. The replacement of three carbonyls by Cp^- in isoelectronic systems has been observed to disable potential inversion for iron,[44] but potential inversion persists when the same change is made to the nonbridging ligands for ruthenium.[28] Calculations on these systems are currently underway in our laboratory. It is tantalizing to speculate that this concept may also relate to the unusual coordination environments of model hydrogenases, which often exhibit potentials that are inverted or nearly so. By utilizing both carbonyls and cyanides in combinations that have been heretofore difficult to understand and by changing the nature of the bridging ligand, the orbital energy matching may be controlled, though much more work is required to verify this hypothesis.

Acknowledgment. We thank the NSF (Grants CHE-0645381 and -0116050) for financial support. M.-H.B. thanks the Research Corp. for a Cottrell Scholarship and the Alfred P. Sloan Foundation for an Alfred P. Sloan Fellowship. R.L.L. thanks Allen Siedle and the Merck Research Corp. for financial support through fellowships.

Supporting Information Available: Tables of structural parameters, Cartesian coordinates, and vibrational frequencies for **1**−**4**, free energy breakdown for reductions in Table 3, orbital plots for **2** and **4**, and detailed energetics for all species and a figure of isosurface plots (0.05 au) and relative energies (eV). This material is available free of charge via the Internet at http://pubs.acs.org.